Long-term trends of ambient nitrate (NO_3^-) concentrations across China based on ensemble machine-learning models

Rui Li[a], Lulu Cui[a *], Yilong Zhao[a], Wenhui Zhou[a], Hongbo Fu[a,b,c *]

[a] *Shanghai Key Laboratory of Atmospheric Particle Pollution and Prevention, Department of Environmental Science & Engineering, Institute of Atmospheric Sciences, Fudan University, Shanghai, 200433, P.R. China*

[b] *Collaborative Innovation Center of Atmospheric Environment and Equipment Technology (CICAEET), Nanjing University of Information Science and Technology, Nanjing 210044, P.R. China*

[c] *Shanghai Institute of Pollution Control and Ecological Security, Shanghai 200092, P.R. China*

*** Correspondence to:**

Drs. H. Fu (Email: fuhb@fudan.edu.cn) and L. Cui (Email: 15110740004@fudan.edu.cn)

Abstract

High loadings of nitrate (NO_3^-) in the aerosol over China significantly exacerbates the air quality and poses a great threaten on ecosystem safety through dry/wet deposition. Unfortunately, limited ground-level observation data makes it challenging to fully reflect the spatial pattern of NO_3^- level across China. Up to date, the long-term monthly particulate NO_3^- datasets at a high resolution were still missing, which restricted the assessment of human health and ecosystem safety. Therefore, a unique monthly NO_3^- dataset at 0.25 ° resolution over China during 2005-2015 was developed by assimilating surface observation, satellite product, meteorological data, land use types and other covariates using an ensemble model combining random forest (RF), gradient boosting decision tree (GBDT), and extreme gradient boosting (XGBoost). The new developed product featured excellent cross-validation R^2 value (0.78) and relatively lower root-mean-square error (RMSE: 1.19 μg N m^{-3}) and mean absolute error (MAE: 0.81 μg N m^{-3}). Besides, the dataset also exhibited relatively

robust performance at the spatial and temporal scale. Moreover, the dataset displayed good agreement with (R^2 = 0.85, RMSE = 0.74 μg N m^{-3}, and MAE = 0.55 μg N m^{-3}) some unlearned data collected from previous studies. The spatiotemporal variations of the developed product were also shown. The estimated NO_3^- concentration showed the highest value in North China Plain (NCP) (3.55 ±1.25 μg N m^{-3}), followed by Yangtze River Delta (YRD (2.56 ±1.12 μg N m^{-3})), Pearl River Delta (PRD (1.68 ±0.81 μg N m^{-3})), Sichuan Basin (1.53 ±0.63 μg N m^{-3}), and the lowest one in Tibetan Plateau (0.42 ±0.25 μg N m^{-3}). The higher ambient NO_3^- concentrations in NCP, YRD, and PRD were closely linked to the dense anthropogenic emissions. Apart from the intensive human activities, poor terrain condition might be a key factor for the serious NO_3^- pollution in Sichuan Basin. The lowest ambient NO_3^- concentration in Tibetan Plateau was contributed by the scarce anthropogenic emission and favorable meteorological factors (e.g., high wind speed). In addition, the ambient NO_3^- concentration showed marked increasing tendency of 0.10 μg N m^{-3}/year during 2005-2014 ($p < 0.05$), while it decreased sharply from 2014 to 2015 at a rate of -0.40 μg N m^{-3}/year ($p < 0.05$). The ambient NO_3^- levels in Beijing-Tianjin-Hebei (BTH), YRD, and PRD displayed gradual increases at a rate of 0.20, 0.11, and 0.05 μg N m^{-3}/year ($p < 0.05$) during 2005-2013, respectively. The gradual increases of NO_3^- concentrations in these regions from 2005 to 2013 were due to that the emission reduction measures during this period focused on the reduction of SO_2 emission rather than NO_x emission and the rapid increase of energy consumption. Afterwards, the government further strengthened these emission reduction measures, and thus caused the dramatic decreases of NO_3^- concentrations in these regions from 2013 to 2015 ($p < 0.05$). The long-term NO_3^- dataset over China could greatly deepen the knowledge about the impacts of emission reduction

measures on air quality improvement. The monthly particulate NO_3^- levels over China during 2005-2015 are open access in https://doi.org/10.5281/zenodo.3988307 (Li et al., 2020c).

1. Introduction

Reactive nitrogen (N_r) emissions displayed remarkable increases in the past decades owing to the high-speed industrial development and urbanization (Cui et al., 2016; Singh et al., 2017). Ambient reactive N emissions were mainly characterized with nitrogen oxides (NO_x), accounting for about 30% of the gross N_r emissions (Chen et al., 2015; Liu et al., 2011). These important N-bearing precursors could be transformed into the nitrate (NO_3^-) via multiple chemical pathways (e.g., heterogeneous or liquid phase reaction), and finally deposited in the terrestrial or aquatic ecosystem (Jia et al., 2016; Qiao et al., 2015; Zhao et al., 2017). On the one hand, heavy loadings of NO_3^- greatly degraded the atmospheric visibility and cool the surface of the Earth system because particulate NO_3^- significantly scattered solar radiation (Fu and Chen, 2017). Moreover, enhanced N deposition might pose a negative effect on the ecosystem health such as biodiversity losses, freshwater eutrophication, and oceanic acidification (Compton et al., 2011; Erisman et al., 2013). Hence, deepening the knowledge about the spatial patterns and long-term trends of particulate NO_3^- in the atmosphere is beneficial to accurately evaluate the ecological and environmental effects of N deposition.

Ground-level observation is often acknowledged to be an effective means to explore the spatial patterns of ambient NO_3^- concentrations. Many long-term monitoring networks including Clean Air Status and Trends Network (CASTNET) and Canadian Air and Precipitation Monitoring Network (CAPMoN) were established to quantify the ambient NO_3^- concentration and inorganic N deposition. Du et al. (2014) revealed that the NO_3^- deposition showed significant decrease across the United

States during 1985-2012 based on these observation data. To date, most of these observation networks focused on North America and Europe, whereas few monitoring sites were located on East Asia especially on China. Fortunately, China has constructed some ground-level observation networks such as CARE-China Observation Network in recent years. On the basis of these observation networks, the overall spatiotemporal trend of particulate NO_3^- concentration has been clarified (Wang et al., 2019c; Xu et al., 2018a). Xu et al. (2018a) observed that the particulate NO_3^- concentration (< 4.5 μm) over China did not show significantly temporal variation during 2011-2015. Very recently, Wang et al. (2019) found that the NO_3^- level in the fine particle ($PM_{2.5}$) decreased by 34% during 2015-2017. Although the overall spatial patterns have been preliminarily revealed based on these isolated sites, these sparse ground-observed sites did not accurately reflect the high-resolution NO_3^- pollution especially the regions far away from these sites because each station only possessed limited spatial representative and NO_3^- concentration was often highly variable in space and time (Liu et al., 2017a). More importantly, the current studies only investigated the ambient NO_3^- concentrations in recent years, while the long-term variation of NO_3^- level remained unknown. It was well known that the energy consumption in China displayed remarkable increase in recent decades (Zhan et al., 2018). Meanwhile, Chinese government also proposed pollutant emission reduction policies since 2005 to ensure the coordinated development of economic growth and environmental protection (Ma et al., 2019). However, the synergistic effects of air pollution control policies and increased energy consumption on long-term evolution trend of NO_3^- pollution over China were not assessed yet, which were extremely critical for the implementation of emission control measures.

To complement the gaps of ground-level observations, satellite product of NO_2 is regarded as a

welcome addition to investigate the long-term trends of N-bearing components in the atmosphere. Ozone Monitoring Instrument (OMI) was regarded as the typical satellite product applied to simulate the ambient NO_3^- concentration (Liu et al., 2017b; Vrekoussis et al., 2013). Jia et al. (2016) firstly used the linear regression method to predict the NO_3^- levels and dry deposition fluxes at the global scale based on OMI-derived NO_2 column amount. However, the dry deposition fluxes of NO_3^- modelled by Jia et al. (2016) showed weak correlation with the measured value ($R = 0.47$), which might be attributable to the simple linear assumption between NO_2 column amount and NO_3^- deposition flux. It was well documented that the nonlinearity relationship between multiple predictors and NO_3^- concentration were hard to reveal on the basis of the simple linear model (Zhan et al., 2018a; Zhan et al., 2018b). To enhance the predictive performance of NO_3^- concentration, Liu et al. (2017) used the chemical transport models (CTMs) to estimate the dry deposition fluxes of N-bearing species recently based on the remotely sensed NO_2 column amount. However, CTMs often suffered from high uncertainty because of the limited knowledge about the generation pathways for particulate NO_3^- in the atmosphere (Zhan et al., 2018a). Recently, the emergence of machine learning models provided unprecedented opportunities to estimate the concentrations of N-bearing components (Chen et al., 2019b; Zhan et al., 2018b). It was well known that the machine-learning models generally showed the better predictive accuracy than CTMs and traditional statistical models when the training samples were sufficient (Zang et al., 2019; Zhan et al., 2017). Zhan et al. (2018b) employed random forest (RF) coupled with spatiotemporal Kriging model to simulate the ambient NO_2 levels over China, and achieved the moderate modelling performance ($R^2 = 0.62$). Afterwards, Chen et al. (2019) used the extreme gradient boosting (XGBoost) model combined with kriging-calibrated satellite method to estimate the national NO_2 concentration and significantly improved

the predictive performance (R^2 = 0.85). Up to date, no study utilized the machine-learning models to significantly improve the predictive accuracy of NO_3^- concentration. Moreover, nearly all of the current studies only focused on the spatial pattern of particulate NO_3^- level in China (Liu et al., 2017; Jia et al., 2016), while they cannot establish a long-term NO_3^- dataset across China.

Here, we firstly developed a high-resolution (0.25°) monthly particulate NO_3^- dataset across China during 2005-2015 based an ensemble model including RF, XGBoost, and gradient boosting decision tree (GBDT) algorithms. At first, the modelling performance and improvement of this new-developed product compared with previous datasets were evaluated. Afterwards, we analyzed the spatial variation and long-term evolution trend of estimated NO_3^- concentration over China and explored the potential impacts of air pollution control measures on NO_3^- variation. The long-term NO_3^- datasets could supply scientific judge for policy makers to mitigate the severe nitrate pollution in China.

2. Input data

2.1 Ground-level NO_3^- data

The monthly NO_3^- monitoring data during 2010-2015 were collected from nationwide nitrogen deposition monitoring network (NNDMN) including 32 sites (Fig. 1, Fig. S1, and Fig. S2), and these sites could be divided into three types including urban, rural, and background sites (Xu et al., 2018a). Ambient concentrations of particulate NO_3^- were determined on the basis of an active DEnuder for Long-Term Atmospheric sampling system (DELTA). The system comprises of a pump, a filter sampling instrument, and a dry gas meter with high sensitivity. Two set of filters in a 2-stage filter pack was applied to sample the aerosol particles, with a first K_2CO_3/glycerol impregnated filter to obtain NO_3^- particles in PM_{10}. All of the monitoring sites kept the same sampling frequency at

the month scale, and these samples were continuously collected over a month. The detailed sampling and analysis procedures have been described by Xu et al. (2018a) and Xu et al. (2019). The detection limit of particulate NO_3^- concentration over China is 0.01 mg N/L.

2.2 Satellite product of NO_2 column density

The OMI-NO_2 level-3 tropospheric column densities (0.25° resolution) were used to predict the NO_3^- concentration (Fig. S3). The OMI aboard on the Aura satellite was available since September, 2004, which displayed global coverage and crossed the entire earth each day. OMI possessed three spectral channels ranging from 270 to 500 nm, and thus was often applied to monitor the gaseous pollutants such as NO_2, SO_2, and O_3.

In this study, we downloaded the daily NO_2 columns during 2005-2015 from https://earthdata.nasa.gov/. The tropospheric NO_2 column density data of poor quality (e.g., cloud radiance fraction > 0.5, solar zenith angles > 85°, and terrain reflectivity > 30%) should be removed. Additionally, the cross-track pixels sensitive to significant row anomaly also must be deleted. Finally, the monthly NO_2 columns were estimated by averaging the daily NO_2 columns.

2.3 Meteorological factors, land use types, and other variables

These independent variables for particulate NO_3^- estimates were gained from multiple sources. The meteorological data on a daily basis (European Centre for Medium-Range Weather Forecasts reanalysis (ECMWF ERA-Interim) datasets (0.25° resolution)) were downloaded from the website of http://www.ecmwf.int/ (Table S1). Among all of the daily meteorological data in ECMWF website, 2-m temperature (T_{2m}), 2-m dewpoint temperature (D_{2m}), 10-m latitudinal wind component (U_{10}), 10-m meridional wind component (V_{10}), sunshine duration (Sund), surface pressure (Sp), boundary layer height (BLH), and total precipitation (Tp) were applied to estimate national NO_3^-

levels. The elevation, gross domestic production (GDP), and population density (PD) data over China were downloaded from the website of http://www.resdc.cn/. PD and GDP in 1995, 2000, 2005, 2010, and 2015 were linearly interpolated to calculate PD and GDP in each year. Then, the yearly GDP data were divided by 12 to estimate the monthly GDP. Afterwards, these data were incorporated into the sub-model to predict the particulate NO_3^- concentration over China. In addition, the land use data (e.g., grassland, forest, urban, and agricultural land) were also downloaded from the website of http://www.resdc.cn/.

These independent variables collected from various sources were uniformly resampled to 0.25° × 0.25° grids. For instance, the land use area, GDP, and PD in 0.25° grid was calculated based on area-weighted average algorithm. To ensure the better predictive performance, it was necessary to employ the appropriate variable selection method to remove some redundant predictors. The basic principle of the variable choice was to remove the variables with the lower importance values. The variables could be regarded as the redundant ones when the R^2 value of the final model showed dramatic decrease after removing them. Based on this method, in the final sub-model, all of the variables except GDP, PD, and grassland have been applied to estimate the ambient NO_3^- concentrations across China.

3. Methods

3.1 Ensemble model development

In the previous studies concerning about air pollution prediction, RF, gradient boosting decision tree (GBDT), and extreme gradient boosting (XGBoost) showed good predictive performance (Li et al., 2020a). RF model possesses a large amount of decision trees, and each one suffered from an independent sampling process and these trees displayed the same distribution (Breiman, 2001). This

model generally shows the higher prediction accuracy due to the injected randomness. The model performance mainly relies on the number of trees, the variable group, and the splitting features. The detailed algorithms are shown as follows:

$$f(x) = \sum_{z=1}^{Z} c_z I(x \in M_z) \quad (1)$$

$$\overset{\Delta}{c}_z = mean(y_i \mid x_i \in M_z) \quad (2)$$

$$L_1(m,n) = \{X \mid X_j \le n\} \,\&\, L_2(m,n) = \{X \mid X_j > n\} \quad (3)$$

$$\min_{m,n}\left[\min \sum_{M_1(m,n)} (y - c_1)^2 + \min \sum_{M_2(m,n)} (y - c_2)^2\right] \quad (4)$$

$$\overset{\Delta}{c}_1 = mean(y_i \mid x_i \in M_1(m,n)) \,\&\, \overset{\Delta}{c}_2 = mean(y_i \mid x_i \in M_2(m,n)) \quad (5)$$

where (x_i, y_i) denotes the sample for i = 1, 2, …, N in M regions (M_1, M_2, …, M_z); I denotes the weight of each branch; L denotes the branch of decision tree; c_m represents the response to the model; $\overset{\Delta}{c}_z$ denotes the best value, m represents the feature variable; c_1 denotes the mean value of left branch; c_2 denotes the mean value of right branch; n is the split point.

GBDT model is often considered to be a typical boosting method. Compared with RF model, each classifier is applied to decrease the residual of the last round. The detailed equations are as follows:

$$c_{tj} = \arg\min \sum_{xi \in Rt_j} L(y_i, f_{t-1}(x_i) + c) \quad (6)$$

$$f_t(x) = f_{t-1}(x) + \sum_{j=1}^{J} c_{tj} I \quad (7)$$

c_{tj} denotes the predicted the estimation error in the last round; R_{tj} denotes each leaf node for the decision trees; yi represents the observed value; $f_{t-1}(x_i)$ is the predicted value in the last round. c was regarded as the optimal value when c_{tj} reaches the least value.

XGBoost method is an updated version of GBDT model and loss functions are expanded to the second order function. On the basis of the pioneering studies (Chen et al., 2019a), XGBoost generally shows excellent performance because of its high efficiency and impressive accuracy. The detailed XGBoost algorithm is shown as the following formula (Zhai and Chen, 2018):

$$L^{(t)} = \sum_{i=1}^{n}[l(y_i, \hat{y}^{(t-1)}) + \partial_{y^{(t-1)}} l(y_i, \hat{y}^{(t-1)}) f_t(x_i) + \frac{1}{2}\partial^2_{y^{(t-1)}} l(y_i, \hat{y}^{(t-1)}) f_t^2(x_i)] + \Omega(f_t) \quad (8)$$

where $L^{(t)}$ represents the cost function at the t-th period; ∂ denotes the derivative of the function; $\partial^2_{y^{(t-1)}}$ denotes the second derivative of the function; l is the differentiable convex loss function that reveals the difference of the predicted value ($\hat{y}$) of the i-th instance at the t-th period and the target value (y_i); $f_t(x)$ denotes the increment; $\Omega(f_t)$ represents the regularizer.

However, each model still shows some disadvantages in the prediction accuracy. Consequently, it was proposed to combine these models with multiple linear regression (MLR) model to further estimate monthly NO_3^- concentration in the atmosphere over China. As shown in Fig. 2, three submodels including RF, GBDT, and XGBoost were stacked through MLR model to estimate the monthly NO_3^- concentration over China. At first, a 5-fold cross-validation method was adopted to train each submodel to determine the appropriate parameter. Afterwards, the MLR model was trained with the final simulated concentrations of three submodels and observations. Finally, the high-resolution ambient NO_3^- level over China were estimated based on the optimal ensemble model. The detailed algorithms are shown as follows (Fig. 2):

$$NO_3^- = \mathrm{A} \times \mathrm{Pred\_RF} + \mathrm{B} \times \mathrm{Pred\_GBDT} + \mathrm{C} \times \mathrm{Pred\_XGBoost} + \mathrm{e}_{ij} \quad (9)$$

where Pred_RF, Pred_GBDT, and Pred_XGBoost denote the predicted NO_3^- concentrations by RF, GBDT, and XGBoost, respectively. A, B, and C represent the partial regression coefficients of RF, GBDT, and XGBoost predictors, respectively. e_{ij} denotes the residual error. Based on the estimates,

the regression coefficients including A, B, C, and the residual error (eij) determined by the MLR model were 0.42, 0.77, 0.09, and -0.87, respectively. The variance inflation factors of RF (2.01), GBDT (2.69), and XGBoost (2.08) were significantly lower than 10, which suggested the MLR model was robust.

The RF model was trained using matlab2019a with a package named random forest-master. Both of GBDT and XGBoost algorithms were conducted using many packages named *gbm*, *caret*, and *xgboost* in R software.

3.2 The error estimation and uncertainty assessment

The estimation performance of the ensemble model was evaluated based on 10-fold cross-validation algorithm. The principle of this method meant that the entire datasets were divided into 10 groups with the same capacity randomly. Nine groups were applied to develop the model and the remained one was used to predict the NO_3^- level. After ten rounds, every observed NO_3^- concentration showed a corresponding predicted value. Some key indices such as determination coefficient (R^2), root mean square error (RMSE), and mean absolute prediction error (MAE) were selected as the key indicators to identify the optimal modelling method.

The uncertainty of ensemble model were mainly derived from input ancillary variables. For instance, both of the satellite data and meteorological data often suffered from some uncertainties. To quantify the uncertainties derived from meteorological data, the meteorological data at 0.25° across China were validated using ground-measured meteorological data downloaded from the website of Chinese Meteorology Bureau (http://data.cma.cn/). Additionally, NO_2 columns generally suffered from some uncertainties, whereas the uncertainties of these NO_2 columns cannot be determined because the data about the ground-level NO_2 columns were not open access. In our study,

242 we only estimated the missing ratio of NO_2 column, thereby evaluating the uncertainty of NO_3^-
243 dataset.

244 3.3 Trend analysis

245 The trend analysis of particulate NO_3^- concentration was performed using the Mann-Kendall
246 nonparametric test. This method has been widely applied to analyze the historical trends of carbon
247 fluxes (Tang et al., 2019) and air quality (Kong et al., 2019), which could reflect whether these data
248 suffered from significant changes at a significance level of 0.05. The detailed calculation process is
249 summarized in Mann (1945) and Kendall (1975).

250 **4. Results and discussion**

251 4.1 Descriptive statistics of observed NO_3^- concentrations

252 The ensemble model were applied to fit the NO_3^- estimation model based on 1636 matched
253 samples across China during 2010-2015. In general, the ground-observed NO_3^- concentration over
254 China ranged from 0.3 μg N m^{-3} in Bayinbrook of Xinjiang province to 7.1 μg N m^{-3} in Zhengzhou
255 of Henan province with the mean value of 2.7 ± 1.7 μg N m^{-3}. The monthly particulate NO_3^-
256 concentrations displayed the highest and lowest values in North China Plain (NCP) and Tibetan
257 Plateau, respectively. Besides, the monthly NO_3^- level exhibited significantly temporal variation
258 during 2010-2015. The ambient NO_3^- concentrations in most of sites displayed the gradual increase
259 during 2010-2014, while they decreased sharply from 2014 to 2015. The spatiotemporal variation
260 of ambient NO_3^- concentration over China shared similar characteristic with NO_2 column amount
261 (Fig. S3). The Pearson correlation analysis revealed that the monthly particulate NO_3^- level showed
262 the significantly positive relationship with NO_2 column amount ($r = 0.57$, $p < 0.01$) and urban land
263 area ($r = 0.35$, $p < 0.05$) (Fig. S4). However, D_{2m} showed the remarkably negative correlation with

ambient NO_3^- concentration ($r = -0.31$, $p < 0.05$).

4.2 The validation of new-developed NO_3^- dataset and comparison with previous products

In our study, the ensemble model was applied to develop a monthly particulate NO_3^- dataset over China based on various predictors. Besides, other three individual models were also trained to compare with their predictive performances. The cross-validation result indicated that the R^2 value of the new product developed by ensemble decision trees model reached 0.78, significantly higher than those developed by RF (0.57), GBDT (0.73), and XGBoost (0.45). Nonetheless, both of RMSE and MAE exhibited the opposite trends. The RMSE value was in the order of XGBoost (1.98 μg N m^{-3}) > RF (1.67 μg N m^{-3}) > GBDT (1.35 μg N m^{-3}) > ensemble model (1.19 μg N m^{-3}). The MAE value followed the similar characteristic with the order of XGBoost (1.29 μg N m^{-3}) > RF (0.99 μg N m^{-3}) > GBDT (0.95 μg N m^{-3}) > ensemble model (0.81 μg N m^{-3}). In some previous studies (Xiao et al., 2018), XGBoost often showed the better performance compared with RF, which seemed to be in contrast to our study. It was assumed that XGBoost showed the better performance for big-data samples. However, the size of training samples in our study was relatively less than those in previous studies. Xiao et al. (2018) also verified that the XGBoost showed the better accuracy than RF in some developed regions such as East China, while RF showed the better performance than XGBoost in Northwest China because the monitoring sites in Northwest China was relatively scarce. Wolpert (1992) suggested the combination of various machine-learning models can significantly strengthen the transferability of models. Chen et al. (2019a) demonstrated that the ensemble model significantly outperformed the individual machine-learning model because the ensemble model can overcome the weaknesses of individual model. Besides, we also assessed the annual modelling performance of NO_3^- estimation. Figure S5 shows that the R^2 value of annual NO_3^- estimation

reached 0.81, slightly higher than monthly NO_3^- prediction (0.78). However, both of RMSE (1.23 μg N m^{-3}) and MAE (0.85 μg N m^{-3}) for annual NO_3^- estimation were slightly higher than those of monthly NO_3^- prediction.

The new developed NO_3^- dataset showed the markedly temporal discrepancy. The R^2 values of NO_3^- estimates during 2011-2015 (0.88, 0.89, 0.83, 0.74, and 0.78) were notably higher than that during 2010 (0.62) (Table 1 and Fig. 3). The relatively lower R^2 value in 2010 attested to the dominant role of sampling size on the predictive accuracy for machine-learning models. The training samples in 2010 (135 samples) were notably less than those in other years due to the lack of observation data in spring. However, both of RMSE and MAE were not sensitive to the sampling size. The higher RMSE and MAE focused on the 2010, 2014, and 2015. The higher RMSE and MAE observed in 2010 might be contributed by the relatively scarce training samples, while the higher RMSE and MAE likely attained to the higher NO_3^- levels during other years. In addition, the performance of the NO_3^- dataset varied greatly at the seasonal scale. The R^2 value was in the order of summer (0.85) > spring (0.80) = autumn (0.80) > winter (0.75) across China (Table 2). The seasonal variation of NO_3^- concentration was in contrast to the results of fine particle modelled by previous studies (Li et al., 2020a; Qin et al., 2018). It was supposed that aerosol optical depth (AOD) was sensitive to the precipitation and relative humidity, and thus showed the worse performance in summer. However, the predictive accuracy of NO_3^- estimation based on NO_2 column amount was closely linked with the chemical transformation from NO_2 to NO_3^-.

The performance of NO_3^- dataset also displayed markedly spatial variation. The highest R^2 value was observed in NCP (0.70), followed by Southwest China (0.60), Southeast China (0.59), Northwest China (0.55), and the lowest one in Northeast China (0.44) (Table 3). The highest R^2

value occurring in NCP was mainly attributable to the largest training samples (> 400) compared with other regions. Southeast China and Southwest China showed satisfactory cross-validation R^2 values because the valid training samples in both of these regions were higher than 300. Although both of Northeast China and Northwest China possessed limited training samples (< 200), the predictive performances of these regions showed significant discrepancy. It was assumed that the sampling sites in Northeast China were very centralized, while the sampling sites in Northwest China were uniformly distributed across the whole region. Geng et al. (2018) revealed that the modelling accuracy based on statistical models were significantly affected by the distribution characteristics of sampling sites. However, both of RMSE and MAE showed different spatial distributions with the R^2 value and slope of fitting curve. Note that the higher values of RMSE and MAE were concentrated on Southwest China (2.08 and 1.41 μg N m^{-3}) and Northwest China (2.06 and 1.38 μg N m^{-3}) rather than NCP (1.74 and 1.06 μg N m^{-3}). There are two reasons responsible for the result. At first, the predictive performances of Southwest China and Northwest China were significantly worse than that of NCP, thereby leading to the higher RMSE and MAE. Moreover, most of the sampling sites in Southwest China were focused on Sichuan Basin, which often showed severe NO_3^- pollution all the year round. Meanwhile, the annual mean NO_3^- concentrations in Yangling and Wuwei reached 4.1 and 4.5 μg N m^{-3}, respectively. The higher loadings of NO_3^- concentrations for training samples led to the higher RMSE and MAE for Northwest China.

Although the cross-validation result suggested the new developed dataset achieved the better modelling accuracy, the cross-validation algorithm cannot test the transferability and agreement of this dataset in the past years. Hence, the unlearned data (annual mean NO_3^- concentration in 10 cities) collected from previous references were employed to validate the transferability of this product. As

shown in Fig. 4 and Table S2, we found that the R^2 value of new-developed NO_3^- product and historical data reached 0.85 (Fig. 4), and the out-of-range R^2 value was even slightly higher than the cross-validation R^2 value. Moreover, the out-of-bag slope based on these unlearning data reached 0.81, and equaled to the slope of cross-validation database. In addition, the site-based cross-validation was also applied to validate the transferability of this dataset. The basic principle is that all of the sites were evenly classified into ten clusters based on the geographical locations. Afterwards, nine of ten were used to train the model and then test the model based on the remained one. After ten round, all of the observed values versus estimate values was considered to be the final result to validate the spatial transferability of this model. As depicted in Fig. S6, the site-based cross-validation R^2 value reached 0.73, which was slightly lower than the cross-validation R^2 value of the training model (0.78). The result suggested the new-developed dataset showed excellent performance in the past decade.

Owing to the severe air pollution issue frequently observed in recent years, especially nitrogen-bearing haze events, many studies have tried to predict the NO_3^- concentrations in China. Most of these studies employed CTMs to simulate the ambient NO_3^- concentrations over China. Huang et al. (2015) employed WRF-CMAQ to estimate the inorganic nitrogen deposition over PRD, and confirmed that the R value only reached 0.54. Afterwards, Han et al. (2017) used RAMS-GMAQ to predict the dry deposition flux of reactive nitrogen, and significantly underestimated the NO_3^- concentration in the atmosphere. Very recently, Geng et al. (2019) used CMAQ to estimate the NO_3^- concentrations over East China, and the predictive performance ($R = 0.53$) showed the similar result to Huang et al. (2015). Apart from these CTMs, the statistical models also has been applied to estimate the ambient NO_3^- concentration over China. Unfortunately, the predictive accuracy was not

good based on traditional statistical models (e.g., linear regression) (R = 0.47) (Jia et al., 2016). In terms of model performance, the developed NO_3^- product in our study was much better than those developed by pioneering studies. Furthermore, this product showed many extra advantages than those obtained by CTMs especially for the estimates of air pollutants. For instance, CTMs generally required continuous emission inventory data, which were often not available and showed high uncertainties. Moreover, CTMs generally needed substantial computing time and big-data input data to ensure the reliable predictive accuracy. Thus, the NO_3^- product retrieved by CTMs often lacks of long-term dataset (> 10 yr), and our study fills the gaps of previous studies.

4.3 Spatial pattern of new-developed NO_3^- dataset

The monthly NO_3^- concentration displayed the similar distribution characteristic with $PM_{2.5}$ and PM_1 (Wei et al., 2019). Overall, the NO_3^- concentration in East China was much higher than that in West China. The higher NO_3^- concentration was concentrated on NCP (3.55 ± 1.25 μg N m^{-3}), followed by Yangtze River Delta (YRD (2.56 ± 1.12 μg N m^{-3})), Pearl River Delta (PRD (1.68 ± 0.81 μg N m^{-3})), Sichuan Basin (1.53 ± 0.63 μg N m^{-3}), and the lowest one observed in Tibetan Plateau (0.42 ± 0.25 μg N m^{-3}) (Fig. 5). Most provinces over NCP such as Beijing, Hebei, Henan, and Shandong suffered from severe NO_3^- pollution due to dense human activities and strong industry foundation (Li et al., 2017) (Fig. S7), which released a large amount of N-bearing gaseous pollutants to the atmosphere especially in winter. In BTH (2.97 ± 1.97 μg N m^{-3}), Wang et al. (2016) verified that these fresh NO_x emitted from power plants or cement industries could be transformed into the nitrate in the particulate phase by the aid of low air temperature. In YRD and PRD, the combustion of fossil fuels and traffic emissions were considered to be the major source of NO_x emission, which favored to the formation of nitrate event through the gas-particle conversion processes (Fu et al.,

2017; Kong et al., 2020; Ming et al., 2017). Apart from the contributions of smelting industries, the poor topographical or meteorological conditions were also responsible for the severe NO_3^- pollution in Sichuan Basin (Tian et al., 2017; Wang et al., 2017). Tibetan Plateau generally showed the clean air quality due to the unique landform and scarce industrial activity (Yang et al., 2018). In addition, it was interesting to note that the Altai region and Taklimakan desert in Xinjiang autonomous region also showed some NO_3^- hotspots, though these regions were often believed to be the remote region. It was assumed that the many petrochemical industries (e.g., Karamai oil field) were located in the Altai region (Liu et al., 2018). Besides, Qi et al. (2018) verified that the resuspension of soil dust might trigger the accumulation of NO_3^- concentration in the aerosol.

4.4 Long-term trend of ambient NO_3^- across China

The temporal variation of NO_3^- levels from 2005 to 2015 over China has been clarified in Fig. 6, Fig. 7 and Table S3. Overall, the ambient NO_3^- concentration in China showed the significant increasing trend of 0.10 μg N m^{-3}/year during 2005-2014, while it decreased sharply from 2014 to 2015 by -0.40 μg N m^{-3}/year. Overall, more than 90% areas of Mainland China showed consistent temporal variation with the gradual increase from 2005 to 2013/2014, and then rapid decrease from 2013/2014 to 2015. However, the decreasing/increasing speed displayed significantly spatial difference in some major regions of China. For instance, the ambient NO_3^- level in BTH showed the remarkable increase during 2005-2013 by 0.20 μg N m^{-3}/year. Afterwards, the NO_3^- level decreased rapidly from 2013 to 2015 at a rate of -0.58 μg N m^{-3}/year. The NO_3^- concentrations in YRD (0.11 μg N m^{-3}/year) and PRD (0.05 μg N m^{-3}/year) both showed the slight increases during 2005-2013, though the statistical test revealed the increases were significant ($p < 0.05$). However, the NO_3^- concentrations in YRD and PRD showed the dramatic decreases with -0.48 and -0.36 μg N m^{-3}/year

396 during 2013-2015, respectively. As seen from 2005 to 2015, the NO_3^- concentration in BTH
397 displayed the slight increase during this period. Nevertheless, the NO_3^- levels in YRD and PRD both
398 displayed the slow decreases by -0.01 and -0.03 μg N m^{-3}/year, respectively.

399 Furthermore, the different provinces displayed disparate temporal variations especially during
400 11th five year plan (2005-2010). 31 provinces (municipalities/autonomous region) of China can be
401 classified into three clusters based on the temporal trends of NO_3^- concentrations during 11th five
402 year plan. The first cluster featured the gradual increase of NO_3^- concentration during this period,
403 which consisted of three provinces in Northeast China (e.g., Heilongjiang) and central provinces in
404 South China (e.g., Jiangxi, Anhui) (Table S3). The second cluster represented the provinces with the
405 stable increases of NO_3^- during 2005-2007 and slight decreases during 2007-2010. Some provinces
406 of NCP (e.g., Beijing, Hebei, Henan) and Northwest China (e.g., Gansu, Inner Mongolia, Ningxia)
407 fell into the second cluster. The last cluster featured the opposite temporal trend to the second cluster
408 during 2005-2010, which included many southern provinces such as Fujian, Guangdong, Zhejiang,
409 and Guangxi. Although the central government proposed the emission reduction goal in 2006, the
410 ambient NO_3^- concentrations in most provinces did not display pronounced decreases, which was
411 totally different from the decrease of $PM_{2.5}$ since 2007 (Xue et al., 2019). Especially in the provinces
412 of Northeast China (e.g., Liaoning), the ambient NO_3^- concentrations in these provinces still showed
413 the rapid increases after the proposal of emission control measures. It was assumed that these
414 provinces generally possessed a large amount of energy-intensive industries and coal-fired power
415 plants (Zhang et al., 2018). Moreover, the result might be associated with the fact that the emission
416 reduction measures focused on the reduction of SO_2 emission rather than NO_x emission (Kanada et
417 al., 2013). Schreifels et al. (2012) revealed that major control measures during this period included

418 shutting down inefficient industries, increasing the pollution levy for excessive SO_2 emissions, and
419 implementing energy conservation projects. Therefore, the total SO_2 emission in 2010 decreased by
420 more than 14% compared with the emission in 1995 and the ambient SO_2 concentrations in many
421 provinces since 2005 displayed significant decreases compared with those in 1990s (Li et al., 2020b;
422 Lu et al., 2013; Zhou et al., 2015). Nonetheless, the NO_x emission in China did not display
423 significant decrease during this period (Duncan et al., 2016; Granier et al., 2017), and thus the
424 ambient NO_3^- in many provinces still kept the higher concentrations. It should be noted that the
425 NO_3^- concentrations in some provinces of NCP exactly exhibited the slow decreases after 2007. It
426 was supposed that the energy structure adjustment and elimination of backward production capacity
427 promoted the small decrease of NO_3^- concentrations (Ma et al., 2019). Unfortunately, the slight
428 decreases were quickly offset by the rapid increase of energy consumption. Zhang et al. (2018)
429 demonstrated that the industry added values and private car number in BTH have been increasing
430 by 189.4% and 279.6% during 2005-2010, respectively. In addition, the decrease of SO_2 emission
431 rather than NO_x emission can further lead to NO_3^- increase because of decreased aerosol acidity,
432 which was dictated by SO_4^{2-} in particulate matter (Xie et al., 2020; Vasilakos et al., 2018).

433 Since 2010, the central government began to implement severe limitations in $PM_{2.5}$, NO_x, and
434 soot emissions, and thus the total NO_x emission during 11th five year plan (2011-2015) showed
435 slow decrease (10%) across China (Ma et al., 2019). However, the NO_3^- concentrations across China
436 did not show rapid response to the emission control measures. For instance, the NO_3^- concentrations
437 in most provinces of China still showed rapid increases during 2010-2013 (2014) (Fig. 7 and Fig.
438 8). The result suggested that the control measures about the NO_x emissions from vehicles and ships
439 might be not very effective. Until 2013, the central government issued Action Plan for Air Pollution

Prevention and Control (APPC-AP) in order to enhance the air pollution prevention measures (Li et al., 2017; Li et al., 2019). Many powerful economic and policy means including pricing (tax) policy and optimization of industrial layout caused the rapid decreases of NO_3^- concentrations after 2013 in many provinces (e.g., Beijing, Hebei, Zhejiang). Wang et al. (2019b) also verified that the NO_3^- level in $PM_{2.5}$ over BTH has decreased by 20% during 2013-2015, which was in accordance with the finding of our study. In addition to the impact of emission reduction, the rapid decrease of NO_3^- concentration over China after 2013 might be linked with the beneficial meteorological factors because Chen et al. (2019c) has demonstrated that favorable meteorological conditions led to about 20% of the $PM_{2.5}$ decrease in BTH during 2013-2015. However, the decreasing trend of NO_3^- concentration during 2014-2015 in PRD (-0.36 μg N m^{-3}/year) was significantly slower than that in BTH (-0.58 μg N m^{-3}/year) and YRD (-0.48 μg N m^{-3}/year) (Table 4). Wang et al. (2019b) found that the ambient NO_3^- concentration in a background site of PRD even showed an upward trend during 2014-2016. Thus, it was necessary to strengthen the control of nitrogen oxide emissions.

In general, the ambient NO_3^- concentration varied greatly at the seasonal scale (Fig. 9). China undergone the most serious NO_3^- pollution in winter (1.57 ± 0.63 μg N m^{-3}), followed by autumn (1.09 ± 0.52 μg N m^{-3}), spring (0.78 ± 0.50 μg N m^{-3}), and the lowest one in summer (0.63 ± 0.40 μg N m^{-3}) (Table S4). The higher NO_3^- concentration observed in winter might be contributed by the dense coal combustion in North China and unfavorable meteorological conditions (Itahashi et al., 2017; Quan et al., 2014; Wang et al., 2019d). The lightest NO_3^- pollution in summer was attributable to the abundant precipitation, which promoted the diffusion and removal of pollutants and reduced ambient NO_3^- level (Hu et al., 2005). The ratio of NO_3^- concentration in winter ($NO_3^-_{winter}$) and that in summer ($NO_3^-_{summer}$) varied greatly at the spatial scale. The $NO_3^-_{winter}$/ $NO_3^-_{summer}$

462 in some provinces (municipalities) including Tianjin (2.11), Hebei (2.25), and Henan (2.84)
463 displayed the higher values compared with other provinces. The higher $NO_3^-{}_{winter}$/ $NO_3^-{}_{summer}$ in NCP
464 might be affected by the fossil fuel combustion for domestic heating, while some southern provinces
465 did not need domestic heating in winter. In contrast, the ratio of $NO_3^-{}_{winter}$/ $NO_3^-{}_{summer}$ exhibited the
466 lower values in some western provinces such as Tibet and Qinghai. It might be probably associated
467 with the less aerosol emission from anthropogenic source and the higher wind speed (Wei et al.,
468 2019).

469 4.5 Uncertainty analysis of NO_3^- estimation

470 The ensemble model of three machine-learning algorithms captured the better accuracy in
471 predicting the NO_3^- level from OMI data. Nonetheless, the ensemble model still showed some
472 improvement space in terms of the R^2 value. At first, meteorological data collected from reanalysis
473 in ECMWF website generally showed high uncertainty, which inevitably increased the error of NO_3^-
474 estimation. In our study, we validated the gridded T_{2m} and Tp datasets against the groud-observed
475 datasets and found that the R^2 values of T_{2m} and Tp reached 0.98 and 0.83 (Table S5), respectively.
476 The result suggested that T_{2m} showed the lower uncertainty, while Tp displayed relatively higher
477 uncertainty. Except T_{2m} and Tp, the ground-level datasets for other meteorological factors were not
478 open access, and thus we cannot assess their uncertainties. Thus, we only reviewed some references
479 and evaluated their uncertainties. For instance, Guo et al. 2019 found that the reanalysis BLH data
480 also exhibited large uncertainties because few sounding data were assimilated. These uncertainties
481 derived from predictors could be passed to the ensemble model, and thus increased the uncertainties
482 of ambient NO_3^- estimates.

483 The second reason was closely linked to the missing NO_2 column amount across China. The

NO_2 column amount retrieval showed many nonrandom biases especially for the arid or semi-arid area with high surface reflectance. The missing NO_2 column amounts over China were not filled in our study due to the increased uncertainty of filling NO_2 column. Moreover, it should be noted that the monthly NO_2 column amounts were averaged based on the daily one, and the missing ratio of daily NO_2 columns during 2005-2015 reached 57.64%, the higher missing ratio might increase the uncertainty of NO_3^- simulation.

Lastly, the developed ensemble model did not integrate the direct spatiotemporal weight indicators (e.g., the distance of observed sites and contiguous grids) though many predictors (e.g., month of year) reflecting spatiotemporal autocorrelation were input into the original model as the key predictors. Furthermore, the developed model was the ensemble one of three original models, which ignored the spatiotemporal autocorrelation of estimation residues from first-stage model. In the future work, the ensemble model could be combined with a space-time model to further enhance the modelling performance.

5. Data availability

The monthly NO_3^- datasets at 0.25° resolution across China during 2005-2015 are available at https://doi.org/10.5281/zenodo.3988307 (Li et al., 2020), which can be downloaded in xlsx format. The missing values are shown in NaN.

6. Conclusions and implications

In this study, RF, GBDT, and XGBoost algorithms were combined to establish a high-resolution (0.25 °) NO_3^- dataset over China during 2005-2015 on the basis of multi-source predictors. The NO_3^- product showed high cross-validation R^2 value (0.78), but low RMSE (1.19 μg N m^{-3}) and MAE (0.81 μg N m^{-3}). The NO_3^- dataset showed the markedly spatiotemporal discrepancy. The R^2 value

was in the order of summer (0.85) > spring (0.80) = autumn (0.80) > winter (0.75) across China, and the R^2 showed the highest value in NCP. In addition, the dataset exhibited excellent transferability (R^2 = 0.85, RMSE = 0.74 μg N m^{-3}, and MAE = 0.55 μg N m^{-3}) on the basis of the unlearning observed data in ten sites.

The new-developed NO_3^- dataset showed remarkably predictive accuracy compared with previous products developed by CTMs and linear regression model. The result might be linked to two key reasons. First of all, the new product assimilated high-resolution NO_2 column amount instead of the NO_x emission inventory used by CTMs. The imperfect knowledge about the chemical modules with regard of the NO_3^- formation and the inaccurate emission inventory decreased the predictive performance of CTMs. In contrast, the new product was obtained using ensemble machine-learning model, which did not need to consider the photochemical or aqueous process from gaseous NO_2 to particulate NO_3^-. Compared with the NO_3^- product estimated by linear regression model (R^2 = 0.21), the new product significantly elevated the modelling performance of NO_3^- concentration. It was supposed that the ensemble model for the development of the new NO_3^- dataset did not predefine the potential relationships between explanatory variables and NO_3^- level as the multiple regression model, which must assume the linear linkage between dependent variable and predictors before model establishment.

On the basis of the such dataset, the spatiotemporal variation of NO_3^- concentration over China during 2005-2015 were clarified. The annual mean NO_3^- concentration followed the order of NCP (3.55 ± 1.25 μg N m^{-3}) > YRD (2.56 ± 1.12 μg N m^{-3}) > PRD (1.68 ± 0.81 μg N m^{-3}) > Sichuan Basin (1.53 ± 0.63 μg N m^{-3}) > Tibetan Plateau (0.42 ± 0.25 μg N m^{-3}). The higher NO_3^- concentrations in NCP, YRD, and PRD were mainly contributed by the intensive industrial and

traffic emissions. Sichuan Basin suffered serious NO_3^- pollution due to the high loadings of aerosols and unfavorable terrain condition. Tibetan Plateau shared with the lightest NO_3^- pollution because of the scarce anthropogenic emissions and favorable meteorological factors. Additionally, we also found that the ambient NO_3^- concentration showed significant increasing trend of 0.10 μg N m^{-3}/year during 2005-2014, while it decreased sharply from 2014 to 2015 at a rate of -0.40 μg N m^{-3}/year. The ambient NO_3^- levels in BTH, YRD, and PRD displayed slight increases at the rate of 0.20, 0.11, and 0.05 μg N m^{-3}/year during 2013-2015, respectively. Afterwards, the NO_3^- concentrations decreased sharply at the speed of -0.58, -0.48, and -0.36 μg N m^{-3}/year. Although National Economic and Social Development of China has issued the emission reduction goal in 2006, the NO_3^- concentrations in most provinces did not show the significant decreases during 2005-2010. It might be contributed by the increase of energy consumption and non-targeted emission control measures. Since 2010, the government began to decrease the NO_x emission over China, whereas the NO_3^- concentrations in many provinces still showed slight increases during 2010-2014 because the benefits of control measures for NO_x emission could be neutralized by elevated energy consumption along with the rapid economic development. Since 2014, Chinese government issued APPC-AP and further enhanced the emission control measures, and triggered the dramatic decrease of NO_3^- concentration over China. Apart from the effect of emission reduction, the favorable meteorological conditions might lead to the rapid decrease of NO_3^- level over China during 2014-2015. Compared with the powerful emission control measures, meteorological factors only contributed a small portion of NO_3^- reduction in China. Besides, the decrease speed of NO_3^- level in China also displayed pronounced spatial heterogeneity and some background region even featured the upward of air pollutant in recent years. Therefore, it is still imperative to strengthen the

emission reduction measures.

It must be acknowledged that our study still suffers from some limitations. First of all, the NO_3^- dataset was developed by machine-learning models, which lacked of the chemical module concerning about the transformation pathway from NO_2 to NO_3^-, and might underestimate the ambient NO_3^- concentration across China. In the future work, the output results of CTMs including conversion ratio from NO_2 to NO_3^-, dry/wet deposition flux of NO_2 and NO_3^- in the atmosphere should be incorporated into the machine-learning model to develop next-generation NO_3^- product. Second, the low time-resolution (monthly) observation data hindered the daily estimation of NO_3^- concentration. The daily NO_3^- datasets are warranted in the future because it could be used to assess the potential impact on human health. Besides, the ultrahigh-resolution satellite (TROPOMI) can allow continuation and enhancement of the spatiotemporal NO_3^- estimation though the OMI product could capture enough spatial variations across China.

Acknowledgements

This work was funded by Chinese Postdoctoral Science Foundation (2020M680589) and National Natural Science Foundation of China (Nos. 21777025).

Author contributions

Rui Li, Lulu Cui, and Hongbo Fu conceived and designed the study. Rui Li, Lulu Cui, Yilong Zhao, Wenhui Zhou collected and processed the data. Rui Li wrote this paper with contributions from all of the coauthors.

References

Breiman, L.: Random forests. Machine learning 45, 5-32, 2001.

Chen, H., Li, D., Gurmesa, G.A., Yu, G., Li, L., Zhang, W., Fang, H., Mo, J.: Effects of nitrogen deposition on carbon cycle in terrestrial ecosystems of China: A meta-analysis. Environ. Pollut. 206, 352-360, https://doi.org/10.1016/j.envpol.2015.07.033, 2015.

Chen, J., Yin, J., Zang, L., Zhang, T., Zhao, M.: Stacking machine learning model for estimating hourly $PM_{2.5}$ in China based on Himawari-8 aerosol optical depth data. Sci. Total Environ. 697, 134021, https://doi.org/10.1016/j.scitotenv.2019.134021, 2019a.

Chen, Z.Y., Zhang, R., Zhang, T.H., Ou, C.Q., Guo, Y.: A kriging-calibrated machine learning method for estimating daily ground-level NO_2 in mainland China. Sci. Total Environ. 690, 556-564, https://doi.org/10.1016/j.scitotenv.2019.06.349, 2019b.

Chen, Z., Chen, D., Kwan, M., Chen, B., Cheng, N., Gao, B., Zhuang, Y., Li, R., and Xu, B.: The control of anthropogenic emissions contributed to 80 % of the decrease in PM2:5 concentrations in Beijing from 2013 to 2017, Atmos. Chem. Phys. Discuss., https://doi.org/10.5194/acp-2018-1112, 2019c.

Compton, J.E., Harrison, J.A., Dennis, R.L., Greaver, T.L., Hill, B.H., Jordan, S.J., Walker, H., Campbell, H.V.: Ecosystem services altered by human changes in the nitrogen cycle: a new perspective for US decision making. Ecology letters 14, 804-815, https://doi.org/10.1111/j.1461-0248.2011.01631.x, 2011.

Cui, S., Shi, Y., Malik, A., Lenzen, M., Gao, B., Huang, W.: A hybrid method for quantifying China's nitrogen footprint during urbanisation from 1990 to 2009. Environ. Interna. 97, 137-145, https://doi.org/10.1016/j.envint.2016.08.012, 2016.

Du, E., de Vries, W., Galloway, J.N., Hu, X., Fang, J.: Changes in wet nitrogen deposition in the United

States between 1985 and 2012. Environ. Res. Lett. 9, 095004, 2014.

Duncan, B.N., Lamsal, L.N., Thompson, A.M., Yoshida, Y., Lu, Z., Streets, D.G., Hurwitz, M.M., Pickering, K.E.: A space-based, high-resolution view of notable changes in urban NO_x pollution around the world (2005–2014). J. Geophy. Res. 121, 976-996, https://doi.org/10.1002/2015JD024121, 2016.

Erisman, J.W., Galloway, J.N., Seitzinger, S., Bleeker, A., Dise, N.B., Petrescu, A.R., Leach, A.M., de Vries, W.: Consequences of human modification of the global nitrogen cycle. Philosophical Transactions of the Royal Society B: Biological Sciences 368, 20130116, https://doi.org/10.1098/rstb.2013.0116, 2013.

Fu, H., Chen, J.: Formation, features and controlling strategies of severe haze-fog pollutions in China. Sci. Total Environ. 578, 121-138, https://doi.org/10.1016/j.scitotenv.2016.10.201, 2017.

Fu, X., Wang, S., Xing, J., Zhang, X., Wang, T., Hao, J.: Increasing ammonia concentrations reduce the effectiveness of particle pollution control achieved via SO_2 and NO_X emissions reduction in east China. Environ. Sci. Tech. Lett. 4, 221-227, https://doi.org/10.1021/acs.estlett.7b00143, 2017.

Georgoulias, A. K., van der A, R. J., Stammes, P., Boersma, K. F., and Eskes, H. J.: Trends and trend reversal detection in 2 decades of tropospheric NO_2 satellite observations, Atmos. Chem. Phys., 6269-6294, https://doi.org/10.5194/acp-19-6269-2019, 2019.

Granier, C., Granier, L., Sindelarova, K., Liousse, C., Darras, S., Bouarar, I., van der Gon, H.D., Frost, G.J., Janssens-Maenhout, G., Crippa, M.: Trends in anthropogenic emissions from 1960 to 2015. Hal. Archives, 2017.

Guo, J., Su, T., Chen, D., Wang, J., Li, Z., Lv, Y., Guo, X., Liu, H., Cribb, M., Zhai, P.: Declining Summertime Local-Scale Precipitation Frequency Over China and the United States, 1981–2012. The

613 Disparate Roles of Aerosols. Geophy. Res. Lett. 46, 13281-13289,
614 https://doi.org/10.1029/2019GL085442, 2019.
615 Han, X., Zhang, M., Skorokhod, A., Kou, X.: Modeling dry deposition of reactive nitrogen in China with
616 RAMS-CMAQ. Atmos. Environ. 166, 47-61, https://doi.org/10.1016/j.atmosenv.2017.07.015, 2017.
617 Hu, M., Zhang, J., Wu, Z.: Chemical compositions of precipitation and scavenging of particles in Beijing.
618 Sci. China B 48, 265-272, Science in China Series B: Chemistry, 2005.
619 Huang, Z., Wang, S., Zheng, J., Yuan, Z., Ye, S., Kang, D.: Modeling inorganic nitrogen deposition in
620 Guangdong province, China. Atmos. Environ. 109, 147-160,
621 https://doi.org/10.1016/j.atmosenv.2015.03.014, 2015.
622 Itahashi, S., Uno, I., Osada, K., Kamiguchi, Y., Yamamoto, S., Tamura, K., Wang, Z., Kurosaki, Y.,
623 Kanaya, Y.: Nitrate transboundary heavy pollution over East Asia in winter. Atmos. Chem. Phys 17,
624 3823-3843, 2017.
625 Jia, Y., Yu, G., Gao, Y., He, N., Wang, Q., Jiao, C., Zuo, Y.: Global inorganic nitrogen dry deposition
626 inferred from ground-and space-based measurements. Sci. Rep. 6, 19810, 10.1038/srep19810, 2016.
627 Kanada, M., Dong, L., Fujita, T., Fujii, M., Inoue, T., Hirano, Y., Togawa, T., Geng, Y.: Regional disparity
628 and cost-effective SO_2 pollution control in China: A case study in 5 mega-cities. Energ. Policy 61,
629 1322-1331, https://doi.org/10.1016/j.enpol.2013.05.105, 2013.
630 Kendall, M.G.: Rank Correlation methods[M] Charles Griffin, London, 1975.
631 Kong, L., Hu, M., Tan, Q., Feng, M., Qu, Y., An, J., Zhang, Y., Liu, X., Cheng, N.: Aerosol optical
632 properties under different pollution levels in the Pearl River Delta (PRD) region of China. J. Environ.
633 Sci. 87, 49-59, https://doi.org/10.1016/j.jes.2019.02.019, 2020.
634 Kong, L., Tang, X., Zhu, J., Wang, Z.F., Li, J.J., Wu, H.J., Carmichael, G.R.: A Six-year long (2013–

635 2018) High-resolution Air Quality Reanalysis Dataset over China base on the assimilation of surface
636 observations from CNEMC. Earth Sys. Sci. Data, https://doi.org/10.5194/essd-2020-100, 2019.
637 Li, R., Cui, L., Hongbo, F., Li, J., Zhao, Y., Chen, J.: Satellite-based estimation of full-coverage ozone
638 (O_3) concentration and health effect assessment across Hainan Island. J. Cleaner Prod. 244, 118773,
639 https://doi.org/10.1016/j.jclepro.2019.118773, 2020a.
640 Li, R., Cui, L., Li, J., Zhao, A., Fu, H., Wu, Y., Zhang, L., Kong, L., Chen, J.: Spatial and temporal
641 variation of particulate matter and gaseous pollutants in China during 2014-2016. Atmos. Environ.
642 161, 235-246, https://doi.org/10.1016/j.atmosenv.2017.05.008, 2017.
643 Li, R., Cui, L., Liang, J., Zhao, Y., Zhang, Z., Fu, H.: Estimating historical SO_2 level across the whole
644 China during 1973–2014 using random forest model. Chemosphere, 125839,
645 https://doi.org/10.1016/j.chemosphere.2020.125839, 2020b.
646 Li, R., Wang, Z., Cui, L., Fu, H., Zhang, L., Kong, L., Chen, W., Chen, J.: Air pollution characteristics
647 in China during 2015–2016: Spatiotemporal variations and key meteorological factors. Sci. Total
648 Environ. 648, 902-915, https://doi.org/10.1016/j.scitotenv.2018.08.181, 2019.
649 Li, R., Cui, L.L., Zhao, Y.L., Zhou, W.H., Fu, H.B.: Long-term trends of ambient nitrate (NO_3-)
650 concentrations across China based on ensemble machine-learning models,
651 https://doi.org/10.5281/zenodo.3988307, 2020c.
652 Liu, L., Zhang, X., Xu, W., Liu, X., Li, Y., Lu, X., Zhang, Y., Zhang, W.: Temporal characteristics of
653 atmospheric ammonia and nitrogen dioxide over China based on emission data, satellite observations
654 and atmospheric transport modeling since 1980. Atmos. Chem. Phys. 17, 9365-9378, 2017a.
655 Liu, X., Duan, L., Mo, J., Du, E., Shen, J., Lu, X., Zhang, Y., Zhou, X., He, C., Zhang, F.: Nitrogen
656 deposition and its ecological impact in China: an overview. Environ. Pollut. 159, 2251-2264,

https://doi.org/10.1016/j.envpol.2010.08.002, 2011.

Liu, X., Xu, W., Duan, L., Du, E., Pan, Y., Lu, X., Zhang, L., Wu, Z., Wang, X., Zhang, Y.: Atmospheric nitrogen emission, deposition, and air quality impacts in China: An overview. Curr. Pollut. Rep. 3, 65-77, 2017b.

Liu, Z., Gao, W., Yu, Y., Hu, B., Xin, J., Sun, Y., Wang, L., Wang, G., Bi, X., Zhang, G.: Characteristics of $PM_{2.5}$ mass concentrations and chemical species in urban and background areas of China: emerging results from the CARE-China network. Atmos. Chem. Phys. 18, 1-34, https://www.atmos-chem-phys.net/18/8849/2018/acp-18-8849-2018-discussion.html, 2018.

Lu, Z., Streets, D.G., de Foy, B., Krotkov, N.A.: Ozone Monitoring Instrument observations of interannual increases in SO_2 emissions from Indian coal-fired power plants during 2005-2012. Environ. Sci. Tech. 47, 13993-14000, https://doi.org/10.1021/es4039648, 2013.

Ma, Z., Liu, R., Liu, Y., Bi, J.: Effects of air pollution control policies on $PM_{2.5}$ pollution improvement in China from 2005 to 2017: a satellite-based perspective. Atmos. Chem. Phy. 19, 6861-6877, https://doi.org/10.5194/acp-19-6861-2019, 2019.

Mann, H.B.: Nonparametric tests against trend Econometrica: J. Econom. Soc., 13, 245-259, 1945.

Ming, L., Jin, L., Li, J., Fu, P., Yang, W., Liu, D., Zhang, G., Wang, Z., Li, X.: $PM_{2.5}$ in the Yangtze River Delta, China: Chemical compositions, seasonal variations, and regional pollution events. Environ. Pollut. 223, 200-212, https://doi.org/10.1016/j.envpol.2017.01.013, 2017.

Qi, J., Liu, X., Yao, X., Zhang, R., Chen, X., Lin, X., Gao, H., Liu, R.: The concentration, source and deposition flux of ammonium and nitrate in atmospheric particles during dust events at a coastal site in northern China. Atmos. Chem. Phys. 18, 571, https://doi.org/10.5194/acp-18-571-2018, 2018.

Qiao, X., Xiao, W., Jaffe, D., Kota, S.H., Ying, Q., Tang, Y.: Atmospheric wet deposition of sulfur and

679 nitrogen in Jiuzhaigou national nature reserve, Sichuan province, China. Sci. Total Environ. 511, 28-
680 36, https://doi.org/10.1016/j.scitotenv.2014.12.028, 2015.
681 Qin, K., Zou, J., Guo, J., Lu, M., Bilal, M., Zhang, K., Ma, F., Zhang, Y.: Estimating PM_1 concentrations
682 from MODIS over Yangtze River Delta of China during 2014-2017. Atmos. Environ. 195, 149-158,
683 https://doi.org/10.1016/j.atmosenv.2018.09.054, 2018.
684 Quan, J., Tie, X., Zhang, Q., Liu, Q., Li, X., Gao, Y., Zhao, D.: Characteristics of heavy aerosol pollution
685 during the 2012-2013 winter in Beijing, China. Atmos. Environ. 88, 83-89,
686 https://doi.org/10.1016/j.atmosenv.2014.01.058, 2014.
687 Schreifels, J.J., Fu, Y., Wilson, E.J.: Sulfur dioxide control in China: policy evolution during the 10th and
688 11th Five-year Plans and lessons for the future. Energ. Policy 48, 779-789,
689 https://doi.org/10.1016/j.enpol.2012.06.015, 2012.
690 Shen, J., Li, Y., Liu, X., Luo, X., Tang, H., Zhang, Y., Wu, J.: Atmospheric dry and wet nitrogen
691 deposition on three contrasting land use types of an agricultural catchment in subtropical central China.
692 Atmos. Environ. 67, 415-424, https://doi.org/10.1016/j.atmosenv.2012.10.068, 2013.
693 Shen, J., Tang, A., Liu, X., Fangmeier, A., Goulding, K., Zhang, F.: High concentrations and dry
694 deposition of reactive nitrogen species at two sites in the North China Plain. Environ. Pollut. 157,
695 3106-3113, https://doi.org/10.1016/j.envpol.2009.05.016, 2009.
696 Singh, S., Sharma, A., Kumar, B., Kulshrestha, U.: Wet deposition fluxes of atmospheric inorganic
697 reactive nitrogen at an urban and rural site in the Indo-Gangetic Plain. Atmos. Pollut. Res. 8, 669-677,
698 https://doi.org/10.1016/j.apr.2016.12.021, 2017.
699 Tang, X.L., Fan, S.H., Du, M.Y., Zhang, W.J., Gao, S.C., Liu, S.B., Chen, G., Yu, Z., Yang, W.N.: Spatial
700 and temporal patterns of global soil heterotrophic respiration in terrestrial ecosystems. Earth Syst. Sci.

Data 12, 1037-1051, 2020.

Tian, M., Wang, H., Chen, Y., Zhang, L., Shi, G., Liu, Y., Yu, J., Zhai, C., Wang, J., Yang, F.: Highly time-resolved characterization of water-soluble inorganic ions in $PM_{2.5}$ in a humid and acidic mega city in Sichuan Basin, China. Sci. Total Environ. 580, 224-234, https://doi.org/10.1016/j.scitotenv.2016.12.048, 2017.

Vasilakos, P., Russell, A., Weber, R., Nenes, A.: Understanding nitrate formation in a world with less sulfate. Atmos. Chem. Phys. 18, 12765–12775, https://doi.org/10.5194/acp-18-12765-2018, 2018.

Vrekoussis, M., Richter, A., Hilboll, A., Burrows, J., Gerasopoulos, E., Lelieveld, J., Barrie, L., Zerefos, C., Mihalopoulos, N.: Economic crisis detected from space: Air quality observations over Athens/Greece. Geophy. Res. Lett. 40, 458-463, https://doi.org/10.1002/grl.50118, 2013.

Wang, H., Shi, G., Tian, M., Zhang, L., Chen, Y., Yang, F., Cao, X.: Aerosol optical properties and chemical composition apportionment in Sichuan Basin, China. Sci. Total Environ. 577, 245-257, https://doi.org/10.1016/j.scitotenv.2016.10.173, 2017.

Wang, Q., Zhuang, G., Huang, K., Liu, T., Lin, Y., Deng, C., Fu, Q., Fu, J.S., Chen, J., Zhang, W.: Evolution of particulate sulfate and nitrate along the Asian dust pathway: Secondary transformation and primary pollutants via long-range transport. Atmos. Res. 169, 86-95, https://doi.org/10.1016/j.atmosres.2015.09.013, 2016.

Wang, W., Xu, W., Wen, Z., Wang, D., Wang, S., Zhang, Z., Zhao, Y., Liu, X.: Characteristics of Atmospheric Reactive Nitrogen Deposition in Nyingchi City. Sci. Rep 9, 1-11, https://xs.scihub.ltd/https://doi.org/10.1038/s41598-019-39855-2, 2019a.

Wang, Y., Li, W., Gao, W., Liu, Z., Tian, S., Shen, R., Ji, D., Wang, S., Wang, L., Tang, G.: Trends in particulate matter and its chemical compositions in China from 2013–2017. Sci. China Earth Sci. 62,

1857-1871, https://xs.scihub.ltd/https://doi.org/10.1007/s11430-018-9373-1, 2019b.

Wang, Y., Li, W., Gao, W., Liu, Z., Tian, S., Shen, R., Ji, D., Wang, S., Wang, L., Tang, G.: Trends in particulate matter and its chemical compositions in China from 2013–2017. Sci. China Earth Sci., 1-15, https://xs.scihub.ltd/https://doi.org/10.1007/s11430-018-9373-1, 2019c.

Wang, Y.L., Song, W., Yang, W., Sun, X.C., Tong, Y.D., Wang, X.M., Liu, C.Q., Bai, Z.P., Liu, X.Y. Influences of atmospheric pollution on the contributions of major oxidation pathways to $PM_{2.5}$ nitrate formation in Beijing. J. Geophy. Res. 124, 4174-4185, https://doi.org/10.1029/2019JD030284, 2019d.

Wei, J., Huang, W., Li, Z., Xue, W., Peng, Y., Sun, L., Cribb, M.: Estimating 1-km-resolution $PM_{2.5}$ concentrations across China using the space-time random forest approach. Remote Sens. Environ. 231, 111221, https://doi.org/10.1016/j.rse.2019.111221, 2019.

Wolpert, D.H.: Stacked generalization. Neural networks 5, 241-259, https://doi.org/10.1016/S0893-6080(05)80023-1, 1992.

Xiao, Q., Chang, H., Geng, G., Liu, Y.: An ensemble machine-learning model to predict historical $PM_{2.5}$ concentrations in China from satellite data. Environ. Sci. Tech. 52, 13260-13269, https://doi.org/10.1021/acs.est.8b02917, 2018.

Xie, Y.N., Wang, G.H., Wang, X.P., Chen, J.M., Chen, Y.B., Tang, G.Q., Wang, L.L., Ge, S.S., Xue, G.Y., Wang, Y.S., Gao, J.: Nitrate-dominated $PM_{2.5}$ and elevation of particle pH observed in urban Beijing during the winter of 2017 Atmos. Chem. Phys. 20, 5019–5033, 2020.

Xu, W., Liu, L., Cheng, M., Zhao, Y., Zhang, L., Pan, Y., Zhang, X., Gu, B., Li, Y., Zhang, X.: Spatial-temporal patterns of inorganic nitrogen air concentrations and deposition in eastern China. Atmos. Chem. Phys. 18, 10931-10954, https://doi.org/10.5194/acp-18-10931-2018, 2018a.

Xu, W., Zhao, Y., Liu, X., Dore, A.J., Zhang, L., Liu, L., Cheng, M.: Atmospheric nitrogen deposition in

745 the Yangtze River basin: Spatial pattern and source attribution. Environ. Pollut. 232, 546-555,
746 https://doi.org/10.1016/j.envpol.2017.09.086, 2018b.
747 Xu, W., Zhang, L., Liu, X.J.: a database of atmospheric nitrogen concentration and deposition from
748 the nationwide monitoring network in China. Sci. Data 6, 51, 2019.
749 Xue, T., Zheng, Y.X., Tong, D., Zheng, B., Li, X., Zhu, T., Zhang, Q.: Spatiotemporal continuous
750 estimates of $PM_{2.5}$ concentrations in China, 2000–2016: A machine learning method with inputs from
751 satellites, chemical transport model, and ground observations. Environ. Interna. 123, 345-357,
752 https://doi.org/10.1016/j.envint.2018.11.075, 2019.
753 Yang, J., Kang, S., Ji, Z.: Sensitivity analysis of chemical mechanisms in the WRF-chem model in
754 reconstructing aerosol concentrations and optical properties in the Tibetan plateau. Aerosol Air Qual.
755 Res. 18, 505-521, doi: 10.4209/aaqr.2017.05.0156, 2018.
756 Zang, L., Mao, F., Guo, J., Wang, W., Pan, Z., Shen, H., Zhu, B., Wang, Z.: Estimation of spatiotemporal
757 $PM_{1.0}$ distributions in China by combining $PM_{2.5}$ observations with satellite aerosol optical depth. Sci.
758 Total Environ. 658, 1256-1264, https://doi.org/10.1016/j.scitotenv.2018.12.297, 2019.
759 Zhai, B.X., Chen, J.G.: Development of a stacked ensemble model for forecasting and analyzing daily
760 average $PM_{2.5}$ concentrations in Beijing, China. Sci. Total Environ. 635, 644-658,
761 https://doi.org/10.1016/j.scitotenv.2018.04.040, 2018.
762 Zhan, Y., Luo, Y., Deng, X., Chen, H., Grieneisen, M.L., Shen, X., Zhu, L., Zhang, M.: Spatiotemporal
763 prediction of continuous daily $PM_{2.5}$ concentrations across China using a spatially explicit machine
764 learning algorithm. Atmos. Environ. 155, 129-139, https://doi.org/10.1016/j.atmosenv.2017.02.023,
765 2017.
766 Zhan, Y., Luo, Y., Deng, X., Grieneisen, M.L., Zhang, M., Di, B.: Spatiotemporal prediction of daily

767 ambient ozone levels across China using random forest for human exposure assessment. Environ.
768 Pollut. 233, 464-473, https://doi.org/10.1016/j.envpol.2017.10.029, 2018a.
769 Zhan, Y., Luo, Y., Deng, X., Zhang, K., Zhang, M., Grieneisen, M.L., Di, B.: Satellite-Based estimates
770 of daily NO_2 exposure in China using hybrid random forest and spatiotemporal Kriging model.
771 Environ. Sci. Tech. 52, 4180-4189, https://doi.org/10.1021/acs.est.7b05669, 2018b.
772 Zhao, Y., Zhang, L., Chen, Y., Liu, X., Xu, W., Pan, Y., Duan, L.: Atmospheric nitrogen deposition to
773 China: A model analysis on nitrogen budget and critical load exceedance. Atmos. Environ. 153, 32-40,
774 https://doi.org/10.1016/j.atmosenv.2017.01.018, 2017.
775 Zhang, X.Y., Zhang, W.T., Lu, X.H., Liu, X.J., Chen, D.M., Liu, L., Huang, X.J.: Long-term trends in
776 NO_2 columns related to economic developments and air quality policies from 1997 to 2016 in China.
777 Sci. Total Environ. 639, 146-155, https://doi.org/10.1016/j.scitotenv.2018.04.435, 2018.
778 Zhou, K., Yang, S., Shen, C., Ding, S., Sun, C.: Energy conservation and emission reduction of China's
779 electric power industry. Renewable and Sustainable Energy Reviews 45, 10-19,
780 https://doi.org/10.1016/j.rser.2015.01.056, 2015.

781 **Fig. 1** Spatial distributions of ground-level NO_3^- monitoring sites used for model establishment. Red

782 circles represent the ground-level sites during 2010-2015. The colormap denotes the elevation

783 distribution across China.

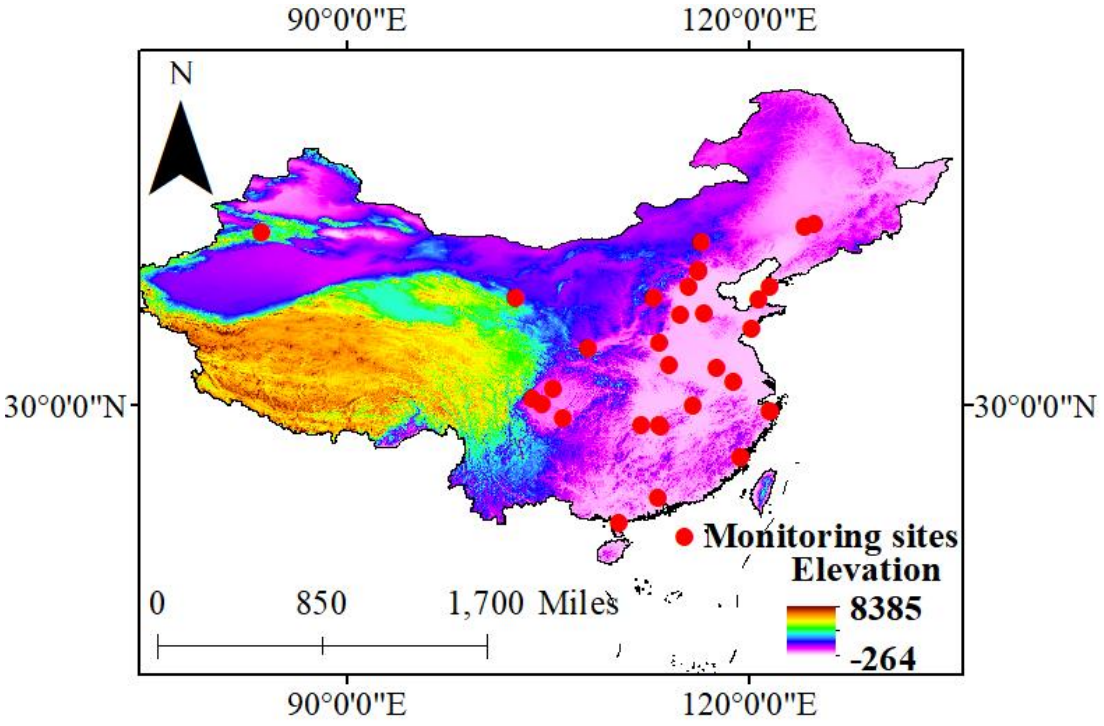

784

785 **Fig. 2** The workflow of the ensemble model development for ambient NO_3^- estimates.

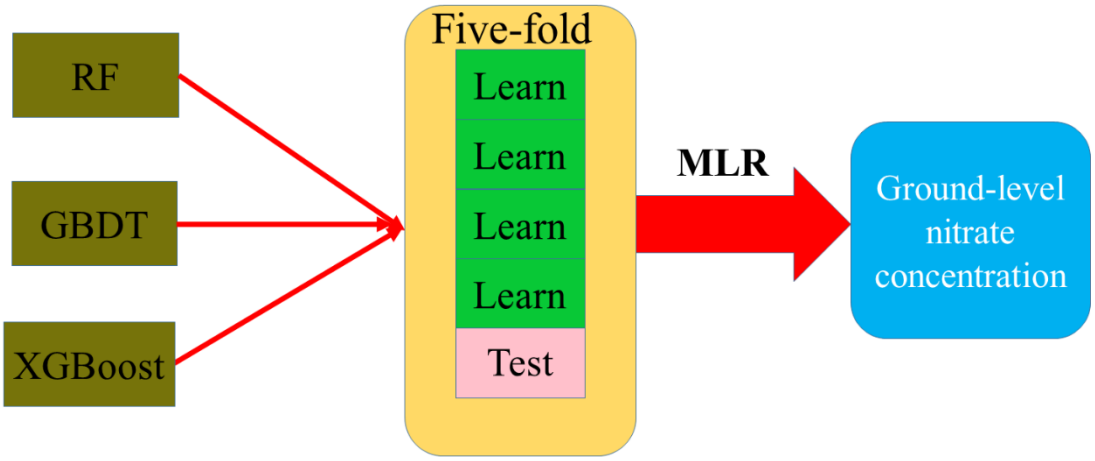

786

Fig. 3 Density scatterplots of 10-fold cross-validation results for monthly NO_3^- estimation (Unit: μg N m-3) across China for the ensemble decision trees model (a), RF (b), GBDT (c), and XGBoost (d), respectively. The color bar reflects the sampling size of each model. The red solid line denotes the best-fit line through the data points (1636 points). The black dashed line denotes the diagonal, which could be used to reflect the deviation of data points.

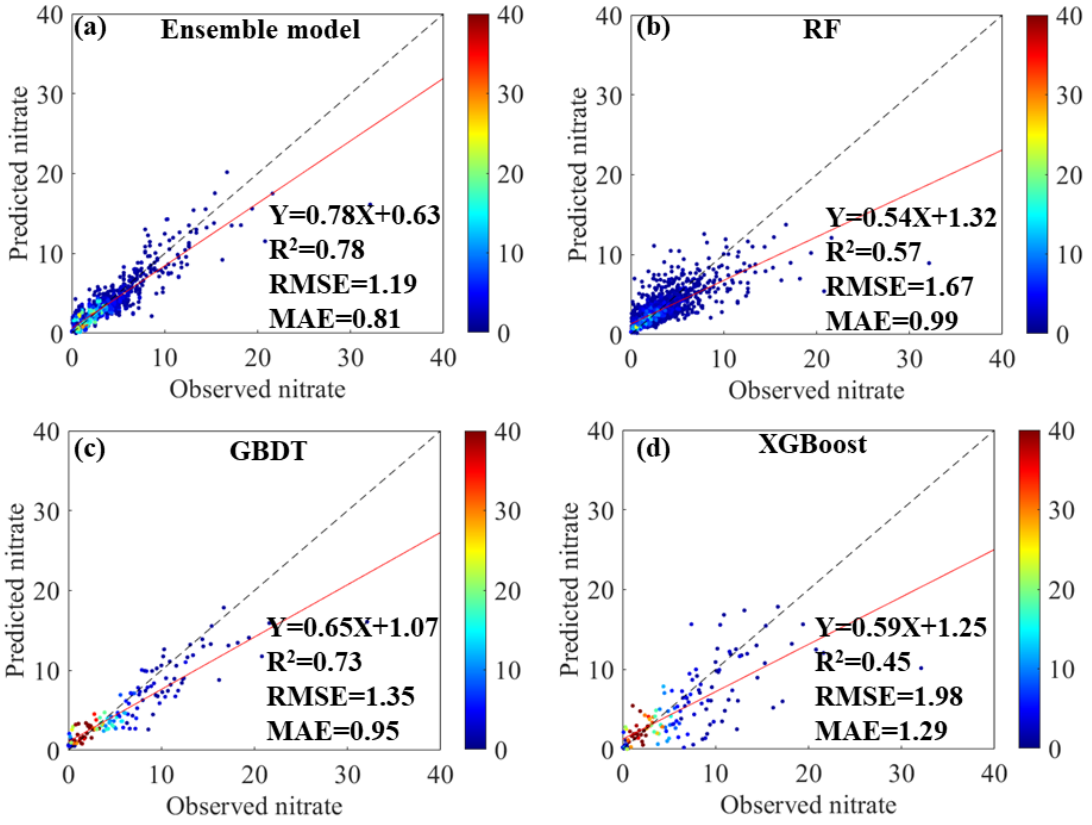

Fig. 4 The transferability validation of the ensemble model in estimating NO_3^- concentration over China based on the unlearning observation data (Shen et al., 2013; Shen et al., 2009; Wang et al., 2019a; Xu et al., 2018b). The color bar reflects the sampling size of each model. The red solid line denotes the best-fit line through the data points. The black dashed line denotes the diagonal, which could be used to reflect the deviation of data points.

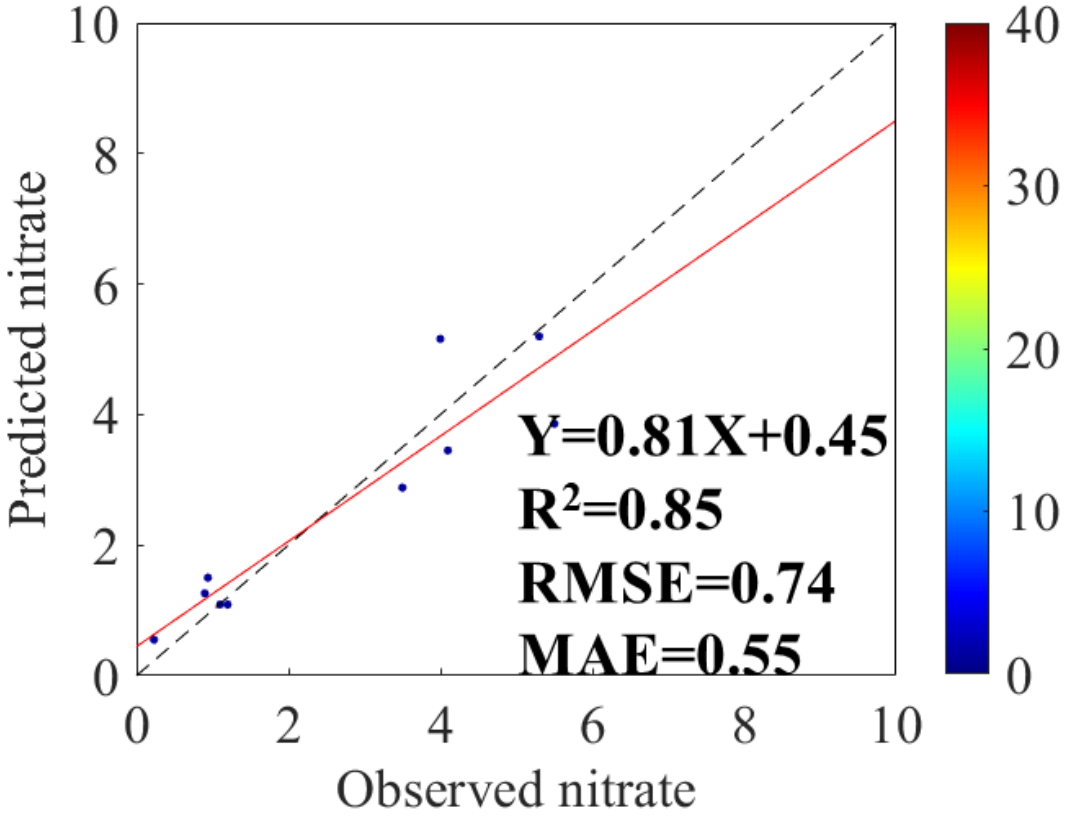

Fig. 5 The spatial pattern of estimated NO_3^- concentration (μg N m^{-3}) over China during 2005-2015 based on the ensemble model.

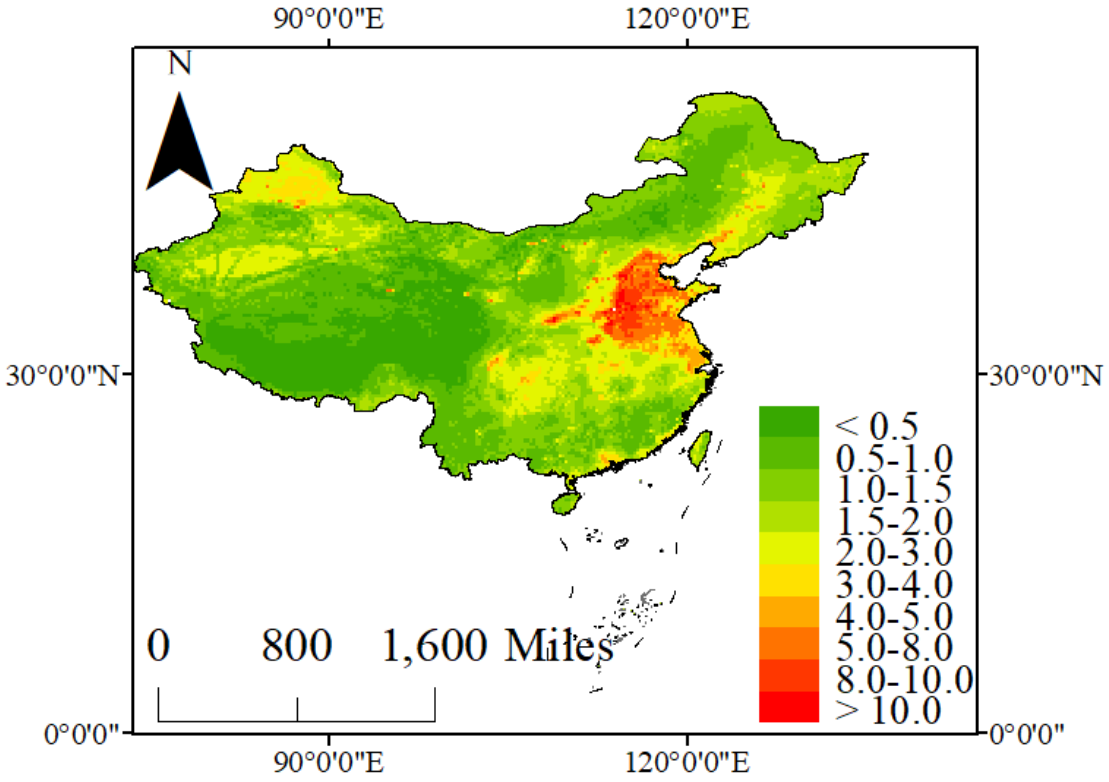

Fig. 6 The annual mean predicted NO_3^- concentrations (μg N m^{-3}) across the entire China from (a)-(k) 2005-2015 based on the ensemble model.

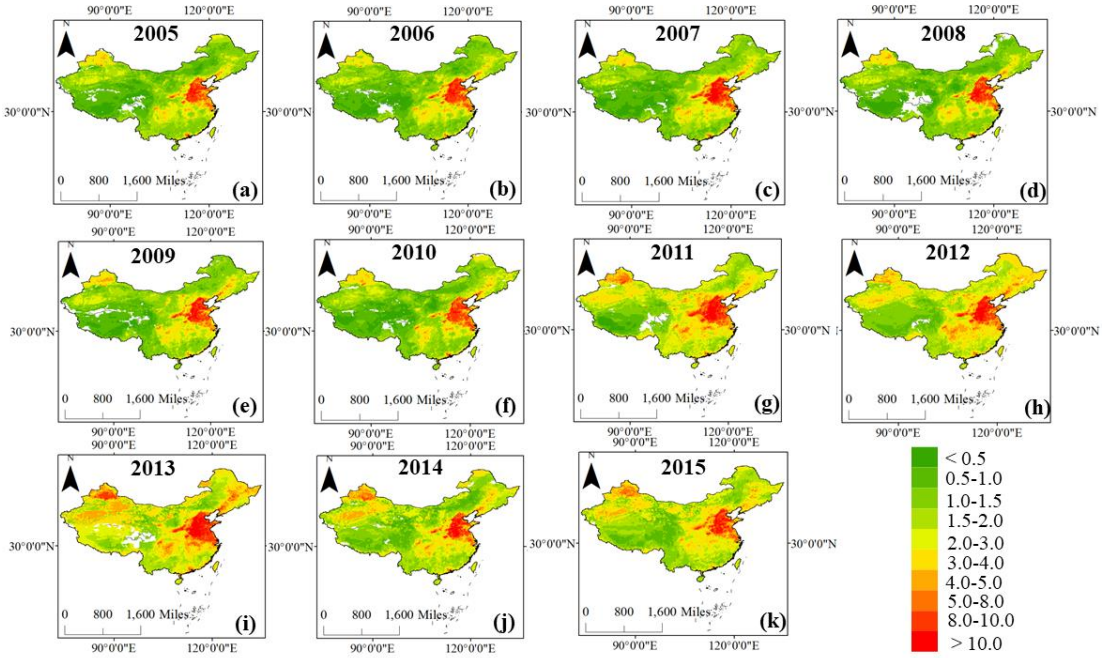

Fig. 7 The annual mean NO_3^- concentrations in major regions across China during 2005-2015. The solid lines denote the mean NO_3^- concentrations and the shadow represents the range of NO_3^- concentrations.

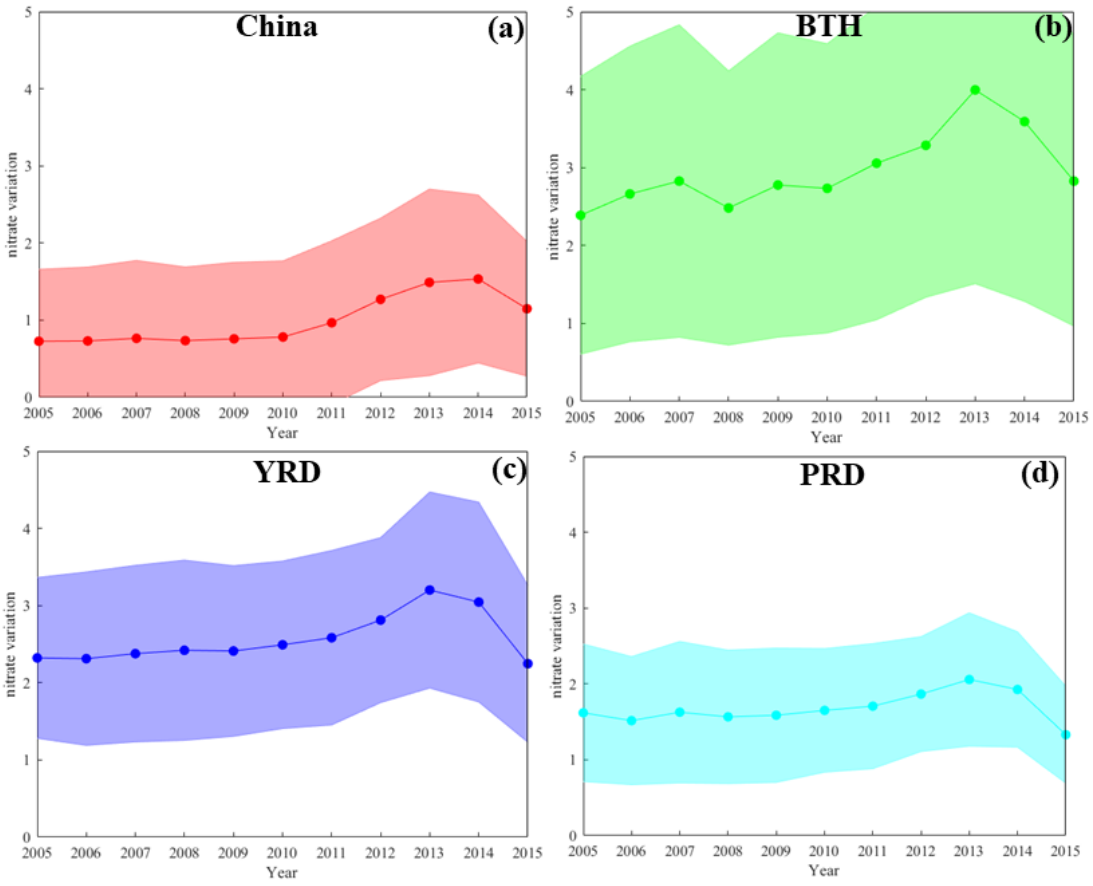

Fig. 8 The long-term trends of NO_3^- concentrations (μg N m^{-3}) and significance levels in China (a, b, and c denote the annual variation of ambient NO_3^- concentration during 2005-2015, 2005-2014, and 2014-2015, respectively. d, e, and f represent the significance level of NO_3^- trend during these periods). The pale green color denotes the regions with the significant variation of ambient NO_3^- concentrations ($p < 0.05$), while the gray color represents the regions with insignificant variation of NO_3^- concentrations.

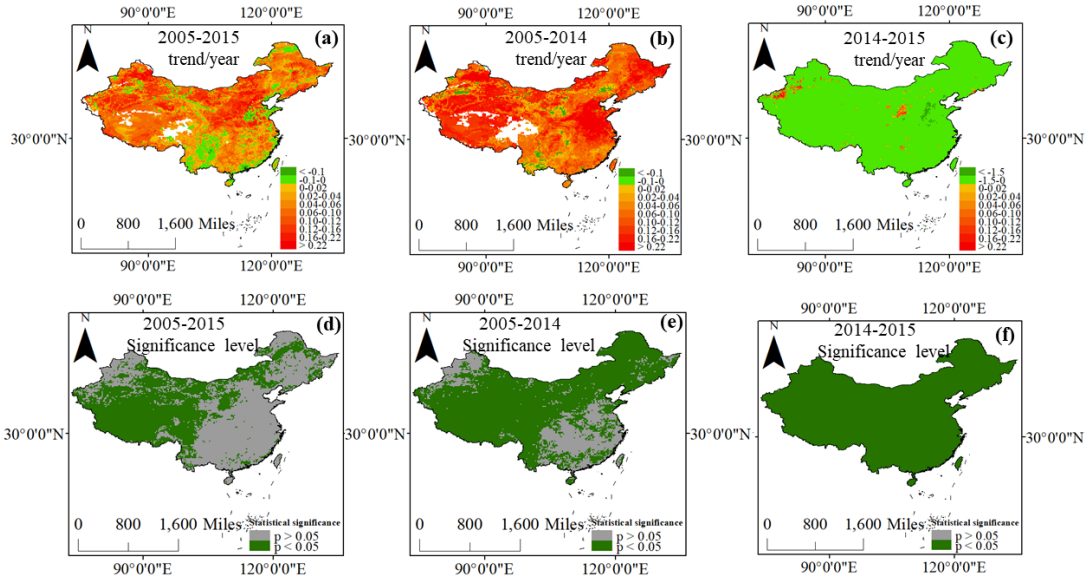

Fig. 9 The mean concentrations of ambient NO_3^- in spring (a), summer (b), autumn (c), and winter (d) during 2005-2015 over China, respectively.

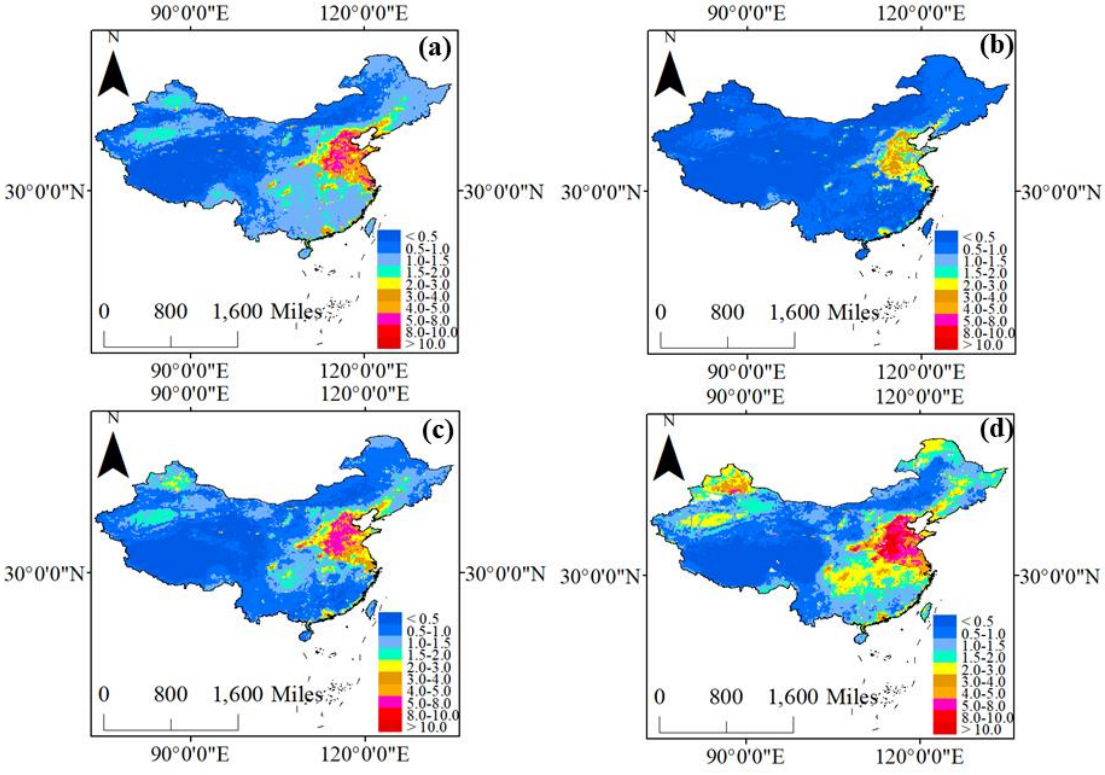

820 **Table 1** The cross-validation result of NO_3^- estimation over China during 2010-2015.

Year	Sample size	R^2 value	Slope	RMSE (μg N m^{-3})	MAE (μg N m^{-3})
2010	135	0.62	0.60	1.39	0.90
2011	291	0.88	0.85	0.32	0.24
2012	274	0.89	0.86	0.33	0.28
2013	312	0.83	0.82	0.64	0.43
2014	306	0.74	0.76	1.50	1.04
2015	318	0.78	0.78	1.35	0.86

821

822 **Table 2** The cross-validation result of NO_3^- estimation over China in four seasons.

Season	Sample size	R^2 value	Slope	RMSE (μg N m^{-3})	MAE (μg N m^{-3})
Spring	395	0.80	0.80	0.71	0.48
Summer	418	0.85	0.84	0.29	0.20
Autumn	437	0.80	0.78	1.10	0.70
Winter	386	0.75	0.73	1.85	1.23

823

Table 3 The cross-validation result of NO_3^- estimation over China in different regions (Northeast China includes Heilongjiang, Jilin, and Liaoning provinces; NCP includes Beijing, Tianjin, Hebei, Henan, Shandong, and Shanxi provinces; Southeast China includes Jiangsu, Zhejiang, Fujian, Guangdong, Jiangxi, Anhui, Hunan, Hainan, Shanghai, and Hubei provinces; Southwest China includes Yunnan, Guangxi, Sichuan, Tibet, Chongqing, and Guizhou provinces; Northwest China includes Inner Mongolia, Xinjiang, Gansu, Qinghai, Ningxia, and Shaanxi.

Season	Sample size	R^2 value	Slope	RMSE (μg N m^{-3})	MAE (μg N m^{-3})
Northeast China	175	0.44	0.43	1.30	0.81
NCP	492	0.70	0.64	1.74	1.06
Southeast China	395	0.59	0.57	1.50	0.84
Southwest China	384	0.60	0.59	2.08	1.41
Northwest China	190	0.58	0.52	2.06	1.38

831 **Table 4** The trend analysis of NO_3^- concentrations in China, BTH, YRD, and PRD regions during
832 2005-2015.

Period	Trend	China	BTH	YRD	PRD
2005-2014	Trend (μg N m^{-3}/year)	0.08	0.13	0.08	0.03
	Significance	$p < 0.05$	$p < 0.05$	$p < 0.05$	$p < 0.05$
2014-2015	Trend (μg N m^{-3}/year)	-0.40	-0.76	-0.79	-0.59
	Significance	$p < 0.05$	$p < 0.05$	$p < 0.05$	$p < 0.05$
2005-2015	Trend (μg N m^{-3}/year)	0.04	0.04	-0.01	-0.03
	Significance	$p < 0.05$	$p > 0.05$	$p > 0.05$	$p < 0.05$

833

834

835